Interlayer Ag Nanoparticle-Anchored Mo, W: BVO/NiCo$_2$O$_4$ Heterojunctions for Synergistic Enhancement of Photoelectrochemical Water Splitting Activity

Wei Zhai, Lin Wang, Shuai Chu, Lei Ding, Jie Li, Haichao Chen*,

Zhengbo Jiao*

Institute of Materials for Energy and Environment, College of Materials Science and Engineering, Qingdao University, Qingdao 266071, P.R. China

Experiment section

Preparation of NiCo$_2$O$_4$ hollow sphere.

Synthesis of SiO$_2$ spheres: 24 mL of ammonia and 81 mL of anhydrous ethanol were mixed and stirred for 5 minutes at room temperature. After thorough stirring, 4.2 mL of tetra-propyl orthosilicate (TPOS) was slowly added to the above solution while being continuously stirred for 1 hour. The resulting product was collected by centrifugation and washed several times with deionized water and ethanol. Finally, the SiO$_2$ spheres were dried at 60 °C under vacuum for 12 hours.

The synthesis of NiCo$_2$O$_4$ hollow microspheres was conducted as follows: Initially, 0.26 g of synthesized SiO$_2$ spheres were dispersed in 70 mL of deionized water and stirred for 10 minutes. Subsequently, 2 mM Co(NO$_3$)$_2$·6H$_2$O and 1 mM Ni(NO$_3$)$_2$·6H$_2$O were added to the above solution, and the mixed solution was continuously stirred for 1 hour to ensure that the Ni and Co metal ions were thoroughly adsorbed onto the surface of the SiO$_2$ spheres. Then, 1.25 g of urea was added to the mixed solution, and the mixture was stirred for an additional hour. After stirring, the NiCo$_2$O$_4$ precursor solution was transferred to a hydrothermal reactor and reacted for 6 hours at 180 °C. At the end of the reaction, the precipitate was collected by centrifugation and the product was washed alternately with deionized water and anhydrous ethanol, and then dried at at 60 °C for 12 hours. Finally, NiCo$_2$O$_4$ hollow microspheres were prepared by heating the NiCo$_2$O$_4$ precursor at a rate of 2 °C/min to 400 °C and annealing for 4 hours. This sample was named NiCo$_2$O$_4$-T.

In addition, $NiCo_2O_4$ samples without the addition of SiO_2 template spheres were also prepared.

Preparation of nano-porous $BiVO_4$ and Mo, W: BVO photoanodes.

First, 75 mM of $Bi(NO_3)_3 \cdot 5H_2O$ and NH_4VO_3 were dissolved in a 10 mL ethylene glycol solvent, separately. Polyethylene glycol (PEG-600) weighing 0.34 g was dissolved in another 10 mL of ethylene glycol solvent. The three solutions were stirred at room temperature and mixed slowly in the ratio (10:10:7) to form the precursor solution of $BiVO_4$. Then, 0.2 mL of the $BiVO_4$ precursor solution was dropped onto an FTO substrate. The sample was dried at 150 ℃ for 60 minutes and annealed at 500 ℃ for 2.5 hours to obtain the $BiVO_4$ photoanode.

The synthesis process of Mo, W: BVO photoanode was similar to that of $BiVO_4$, except that $(NH_4)_{10}H_2(W_2O_7)_6$ and $(NH_4)_6Mo_7O_{24}$, with W and Mo ionic contents of 3% each, were added to the ethylene glycol solvent containing NH_4VO_3.

Preparation of Mo, W: $BVO/NiCo_2O_4$/Ag NPs photoanode.

0.1 mL of the Mo, W: BVO precursor solution was dropped onto an FTO substrate. The sample was dried and annealed. Then, the Mo, W: BVO photoanode was immersed in a 0.1 mM solution of $AgNO_3$ and then irradiated for 10 minutes on an A.M 1.5G filter (Xenon lamp, XQ 300W). The resulting Mo, W: BVO photoanode were then rinsed with deionized water and dried in air to obtain Mo, W: BVO/Ag NPs substrate. The nano-porous Mo, W: $BVO/NiCo_2O_4$/Ag NPs thin film mentioned here is prepared

through the process of solid-state solution drying and calcination (SSDC). Specifically, a certain amount of $NiCo_2O_4$ powder is first added to the Mo, W: BVO precursor solution and then stirred for one hour to form a homogeneous solution. Next, 0.2 mL of the Mo, W: $BVO/NiCo_2O_4$ mixed solution is dropped onto an existing Mo, W: BVO/Ag NPs substrate, followed by drying and calcination, in the same method as for Mo, W: BVO preparation.

Similarly, the preparation process of Mo, W: $BVO/NiCo_2O_4$ is similar, with the main difference that the deposition of Ag NPs is not involved on the surface of the Mo, W: BVO photoanode. It should be noted that this method aims to simplify the required coating steps and improve production efficiency in order to prepare high-quality nano-porous Mo, W: $BVO/ NiCo_2O_4$/Ag NPs thin films in a more efficient manner.

Characterization

The crystal structure and phase of samples were identified by X-ray diffraction (XRD, Rigaku Ultima IV instrument) with Cu Kα radiation (40 KW), and recorded from 10° to 90° with a scanning rate of 0.0678 s^{-1}. The morphology and structure of the samples were analyzed by Scanning electron microscopy (SEM, JSM-7800F. JEOL) and a Transmission electron microscope (TEM, JEOL, JEM-2100 Plus). X-ray photoelectron spectroscopy (XPS) measurements the elements valence using the PHI 5000 Versa Probe III. Ultraviolet and visible spectrophotometry (UV-vis) absorption spectra were measured by UV-2550 (Shimadzu) with $BaSO_4$ as the background. The photoluminescence (PL) emission spectra were measured with an excitation

wavelength of 360 nm by FS5. PEC tests were performed with a standard three-electrode system on an electrochemical workstation (CHI 660e).

Photoelectrochemical measurements

All photoelectrochemical (PEC) tests were conducted in a standard three-electrode system (CHI-660D electrochemical analyzer, Shanghai Chenhua). All BVO-based photoanodes were illuminated from the front side. The light source used was a simulated solar light AM 1.5G (100 mWcm^{-2}, NBeT, HSX-F300). The electrolyte used for the tests was a 0.1 M Na_2SO_4(pH=7) solution. In this study, all potentials were converted to reversible hydrogen electrode (RHE) using the equation, and the conversion relationship between electrochemical reversible hydrogen electrode (RHE) and saturated calomel electrode (SCE) can be expressed by the following formula:

$$E\,(vs\,RHE)\,=\,E\,(vs\,SCE)\,+\,0.0591\,pH\,+\,0.210\,V$$

In which, E (vs RHE) is the potential relative to RHE, E (vs SCE) is the potential relative to SCE, and pH represents the acidity or alkalinity of the solution (expressed as a negative logarithm).

The applied bias photon-to-current efficiency (ABPE) was calculated according to the equation[1]:

$$ABPE = \frac{J(1.23V - V_{RHE})}{P_{light}} \times 100\%$$

where J is the photocurrent density obtained at the applied bias (V vs RHE) and Plight is the incident illumination intensity.

The incident photon-electron conversion efficiency (IPCE) of the samples was

measured using a 300 W xenon lamp and a monochromator (71SWS, Beijing Seven Star Optical Instruments Co., Ltd.) is under monochromatic illumination at a bias voltage of 1.23 V[2]:

$$IPCE = \frac{1240 \times J}{\lambda \times P_{light}} \times 100\%$$

where λ is the incident light wavelength (nm), P_{light} is the power density of monochromatic light at each wavelength (mW·cm^{-2}), J presents the photocurrent density (mA·cm^{-2}).

Electrochemical impedance spectroscopy Nyquist plots were conducted in the frequency range of 10^{-1} to 10^5 Hz, with an AC amplitude range of 5 mV. The measured impedance data was also fitted to an appropriate equivalent circuit using the Z-view software package to obtain the corresponding resistance values. Under dark conditions, Mott-Schottky (M-S) curves were obtained at a frequency of 1 kHz in the potential range of -1 to 0.5 V vs SCE. The formula for calculating the carrier concentration is as follows[3]:

$$N_d = \left(\frac{2}{q\varepsilon\varepsilon_0}\right) \times \left[\frac{d\left(\frac{1}{c^2}\right)}{dv}\right]^{-1}$$

The electron charge q and the vacuum permittivity ε_0 are 1.6×10^{-19} C and 8.85×10^{-14} F·cm^{-1}, respectively. ε is the relative permittivity of $BiVO_4$ ($\varepsilon = 68$), and $d(1/C^2)/dv$ is the slop of the obtained M-S curve.

Surface charge transfer efficiency (η_{tra}) can be calculated by the following[4]:

$$\eta_{tra} = \frac{J_{H_2O}}{J_{Na2SO3}} \times 100\%$$

J_{H2O} and J_{Na2SO3} are the photocurrent density without and with Na_2SO_3 hole scavenger, respectively.

The quantization using parameter D is calculated as follows[5]:

$$D = \frac{I_t - I_s}{I_m - I_s}$$

where I_t, I_s and I_m are the time-dependent photocurrent, the steady-state photocurrent and the transient photocurrent spike, respectively. The electron lifetime (τ_r) is defined as the time at which $lnD = -1$.

The band gap estimation formula for different samples is calculated as follows[6]:

$$(\alpha h v)^n = A (h v - E_g)$$

where α is the absorption coefficient, hv is the photon energy, A is a constant(A=1), E_g is the optical band gap energy, and n is equal to 1/2 for an indirect band gap and 2 for a direct band gap.
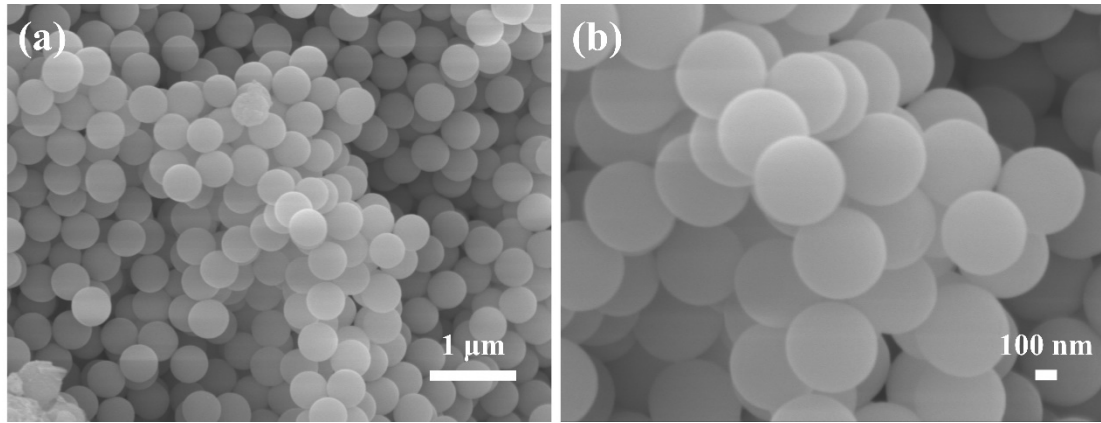
Fig.S1. SEM images of SiO$_2$.
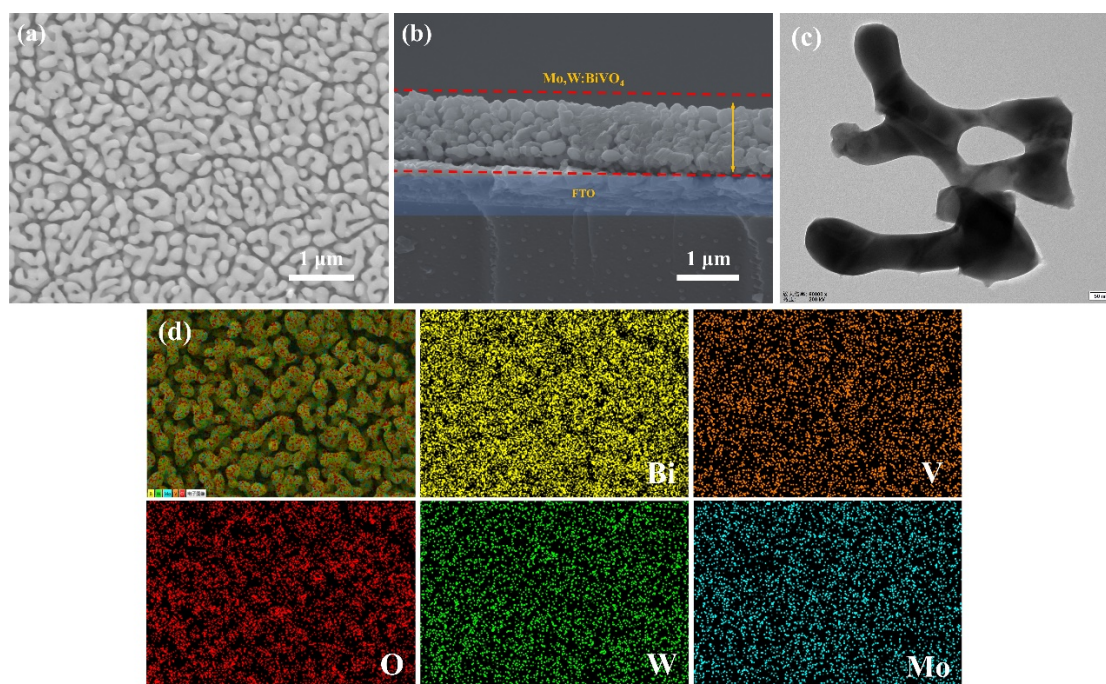
Fig.S2. (a) Top SEM image and (b) Cross section image of nano-porous Mo, W: BVO on FTO substrate, (c) TEM image of Mo, W: BVO, (d) EDS mapping of Mo, W: BVO.
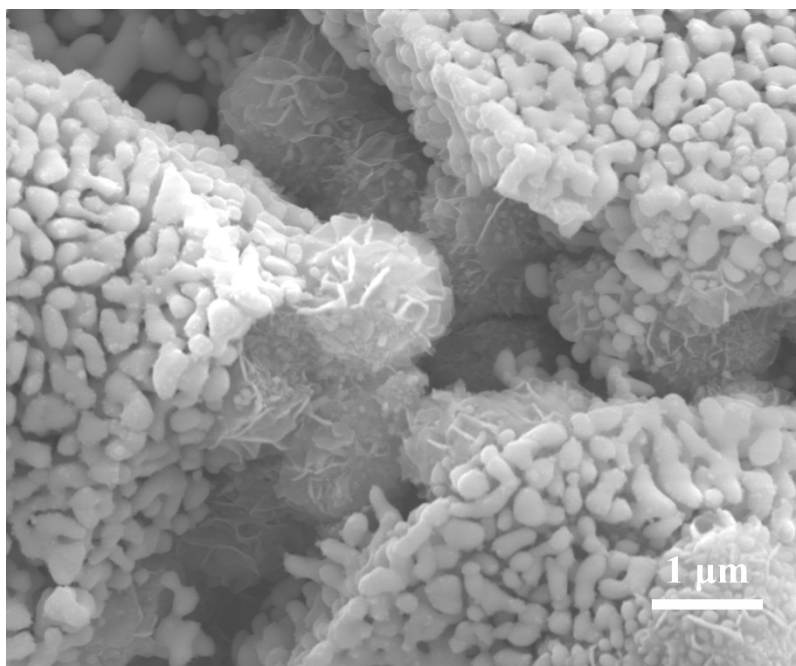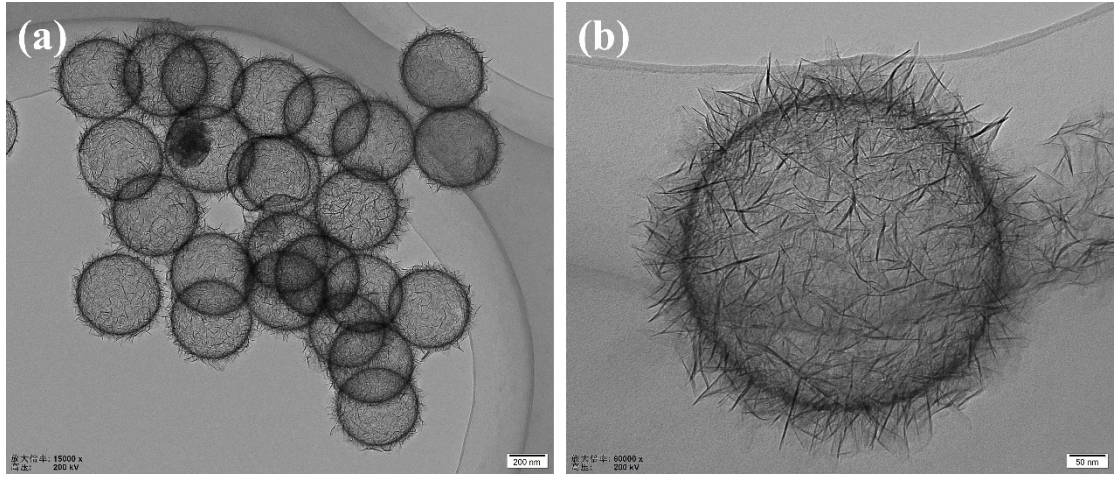
Fig.S3. SEM images of Mo, W: BVO/NiCo$_2$O$_4$/Ag NPs.
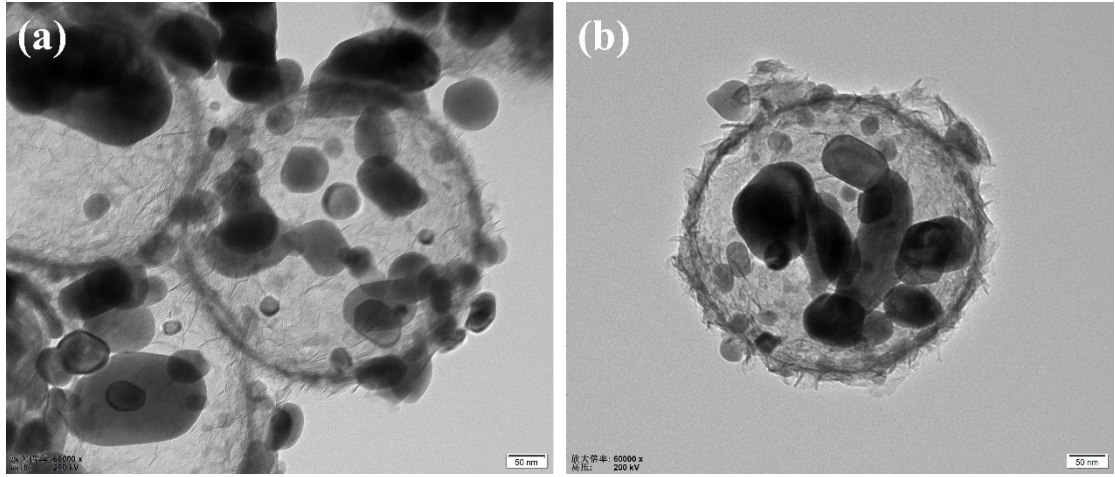
Fig.S4. TEM images of NiCo$_2$O$_4$.

Fig.S5. TEM images of Mo, W: BVO/NiCo$_2$O$_4$/Ag NPs.
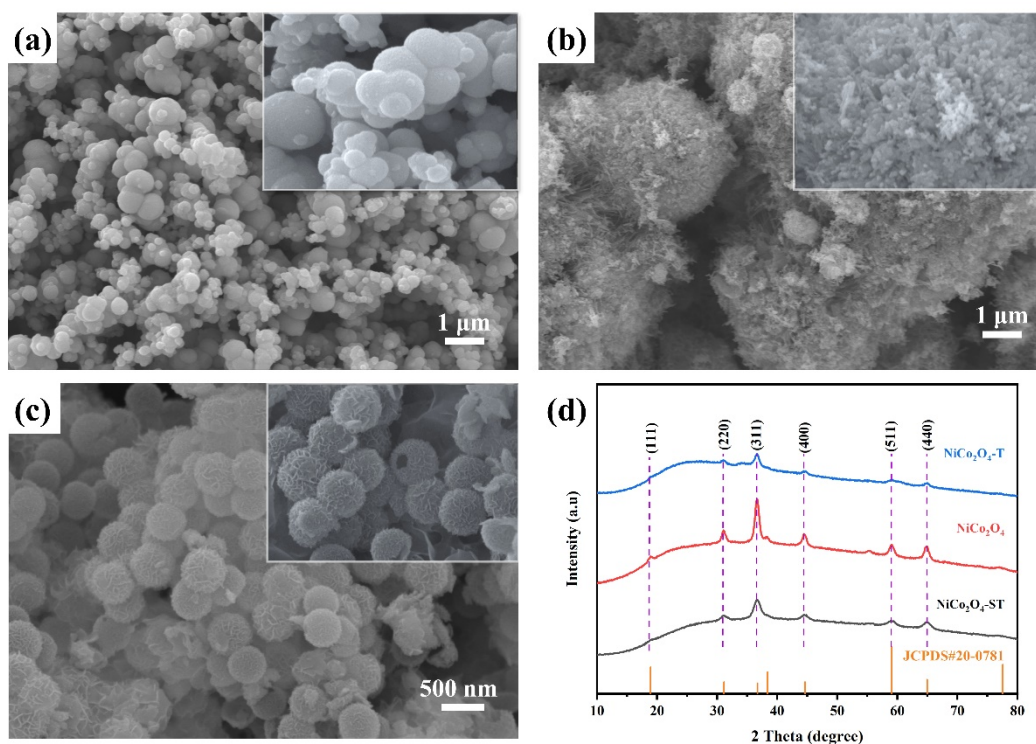
Fig.S6. SEM images of NiCo$_2$O$_4$ synthesized by different methods. (a) self-template, (b) no template, (c) hard-template. (d) XRD patterns of the as-prepared NiCo$_2$O$_4$.

Fig.S6a illustrates the use of Ni-Co glycerate solid spheres as self-templates for NiCo$_2$O$_4$ synthesis. The inset shows that NiCo$_2$O$_4$ presents itself in an irregular spherical shape. In contrast, the synthesis method in **Fig.S6b** follows the same steps as the template method but with no SiO$_2$ template. The inset shows that NiCo$_2$O$_4$ takes on a disordered nanosheet morphology. This unique structure **Fig.S6c** has a distinct advantage over the previous two structures, as it promotes electron-hole pair separation, suppressing charge carrier recombination. Additionally, the hollow structure provides an excellent platform for loading with BVO, which is incomparable to the other two methods. The XRD of the synthesized NiCo$_2$O$_4$ can correspond well to the spinel structure of NiCo$_2$O$_4$ (JCPDS#20-0781), as shown in **Fig.S6d**.
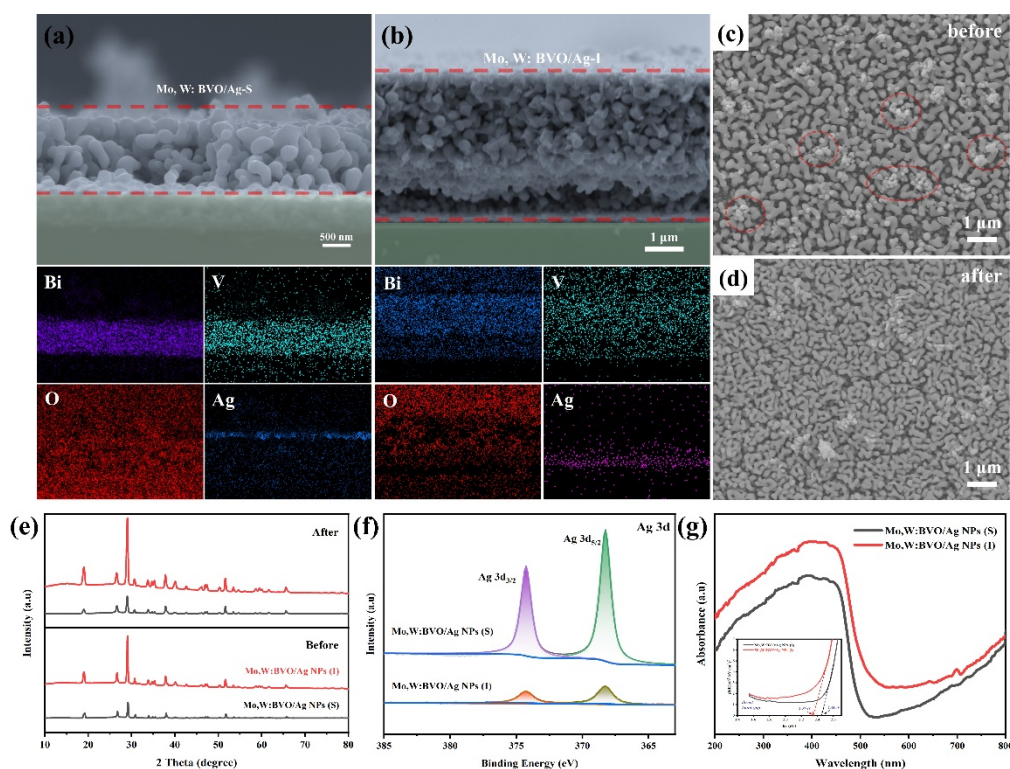
Fig.S7. Side elemental Mapped images of Ag NPs deposited in different locations (a) Surface, (b) interlayer, the SEM images of Mo, W: BVO/Ag NPs-S photoanodes (c) before reaction, (d) after reaction, (e) XRD patterns of Mo, W: BVO/Ag NPs, (f) XPS spectra of Mo, W: BVO/Ag NPs, (g) UV-visible diffusive reflection spectra of Mo, W: BVO/Ag NPs.

The side-view elemental mapping of Ag NPs at different positions on Mo, W: BVO is presented in **Fig.S7(a-b)**, revealing the distribution of Ag on the surface and within the middle of Mo, W: BVO based on the Ag element mapping. To gain further insight into the oxidation degree of Ag NPs, examination of the morphological changes of Mo, W: BVO/Ag NPs-S before and after electrochemical testing **Fig.S7(c-d)** indicates a phenomenon of Ag NPs oxidation and detachment during the electrochemical testing process. In addition, XRD analysis of samples at different deposition positions before and after electrochemical testing as shown in **Fig.S7e**,

revealed that all diffraction peaks could be attributed to $BiVO_4$, and no corresponding Ag diffraction peaks were observed, indicating that the deposition of Ag did not alter the structure of $BiVO_4$. Surface chemical states of Ag deposition were studied by XPS, and the Ag 3d high-resolution spectrum in **Fig.S7f** showed binding energies of 368.25 and 374.25 eV for Ag $3d_{5/2}$ and Ag $3d_{3/2}$, respectively. It should be noted that the relative content of Mo, W: BVO/Ag NPs-I was lower compared to Mo, W: BVO/Ag NPs-S. Using UV-Vis diffuse reflectance spectroscopy (**Fig.S7g**), we found that the deposition of Ag NPs significantly enhances the light-harvesting ability of Mo, W: BVO, which is mainly attributed to the surface plasmon resonance (SPR) effect of Ag NPs. For the Mo, W: BVO/Ag NPs-I samples, we observed a significantly enhanced optical absorption performance in the visible region compared to Mo, W: BVO/Ag NPs-S. In addition to the redshift at the absorption edge, the Ag NPs in the interlayer can provide a chemical environment that avoids oxidation, unlike the Ag NPs in the surface state, which is very effective for visible light trapping and excitation of the local surface plasma.
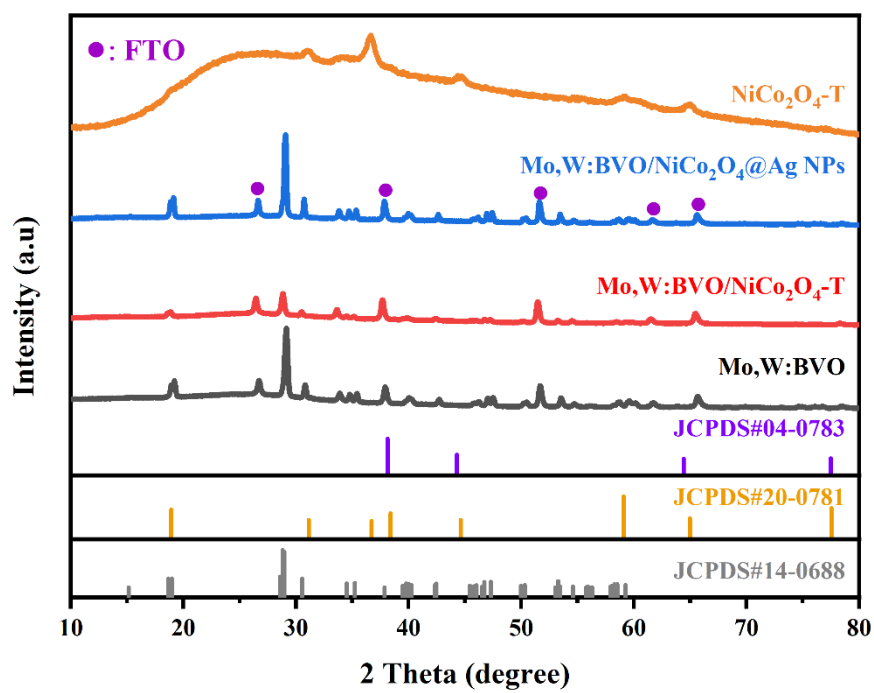
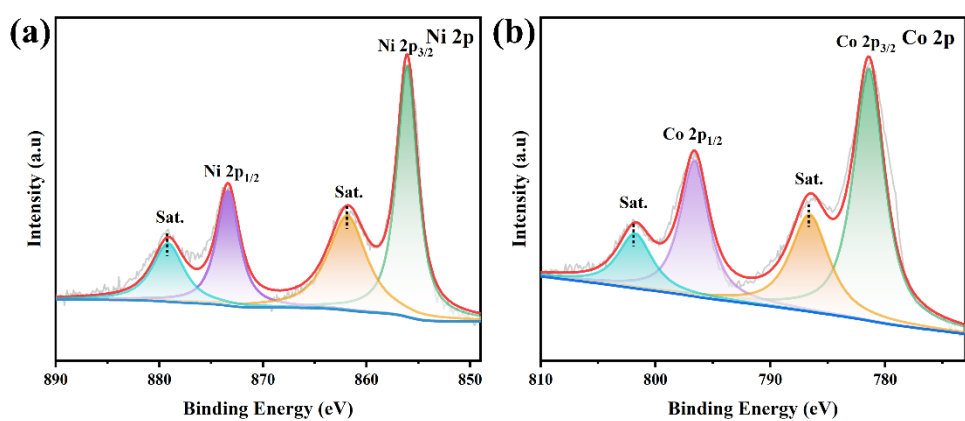**Fig.S8.** XRD patterns of Mo, W: BVO-based samples.

Fig.S9. High resolution XPS spectrum of (a) Ni 2p and (b) Co 2p collected from NiCo$_2$O$_4$.

Compared to Mo, W: BVO/NiCo$_2$O$_4$/Ag NPs, the Ni and Co XPS signals for pristine NiCo$_2$O$_4$ can be clearly to see.
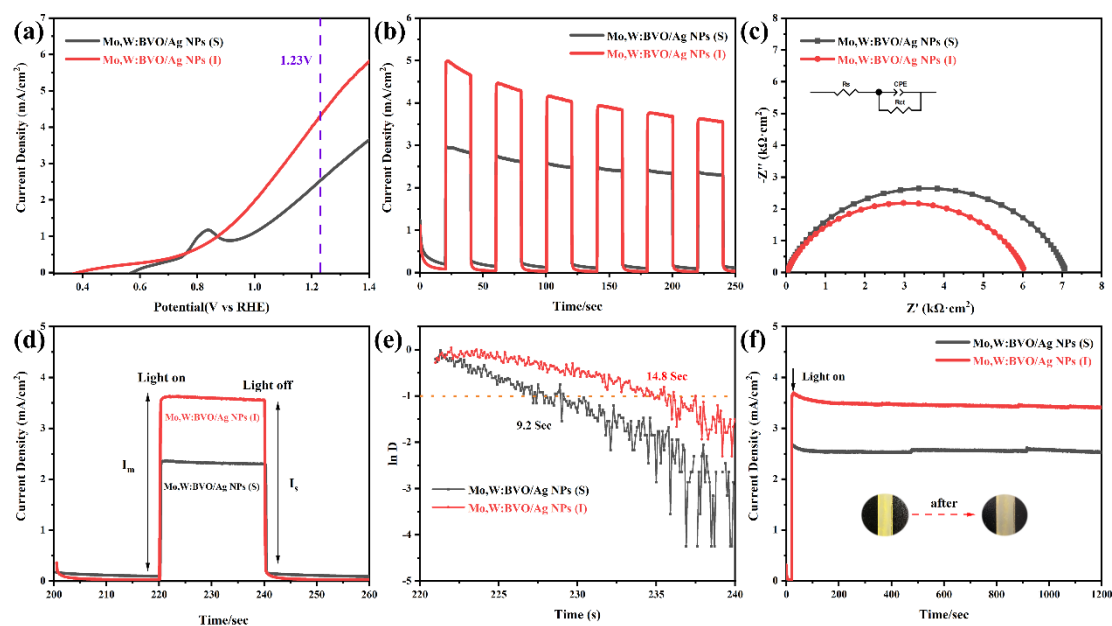
Fig.S10. (a) Liner-sweep voltammograms (LSV, with a scan rate of 50 mV^{-1}), (b) i-t stability tests measured, (c) Nyquist plots of the EIS spectra (d) the transient photocurrent curves and (e) transient decay time of the as-obtained photoanodes, (f) photocurrent stability test. All the measurements were carried in 0.1 M Na$_2$SO$_4$ (pH=7) electrolyte.

We believe that this difference is mainly due to the difference in the surface plasmon resonance (SPR) effect caused by the positional distribution of the Ag NPs. The influence of the SPR effect of Ag NPs transfers energy to metal semiconductors through hot electron transfer and plasmon resonance, thereby enhancing the photoelectrochemical properties. Therefore, the distribution of Ag NPs positions determines the importance of their role in semiconductors. The interlayer distributed Ag NPs have a better contact area and shorter energy transfer channel with Mo, W: BVO and NiCo$_2$O$_4$, while Ag NPs in the surface state suffer from detachment during water oxidation. Therefore, it is a better choice to embed Ag NPs into the composite

structure and construct a sandwich nanocomposite structure to provide a stable chemical environment for Ag NPs. In addition, the SPR effect embedded in Ag NPs induces the enhancement of the internal electric field of the semiconductor. This process not only promotes the accumulation of charge carriers, but also contributes to the rise of the charge concentration of the two semiconductors, greatly reducing the recombination of photogenerated electron-hole pairs. . Its optical properties were evaluated by UV-vis. Due to the embedding of Ag NPs, Mo, W: BVO/Ag NPs-I showed better photo-response than Mo, W: BVO/Ag NPs-S. By collecting the photocurrent density distributed at different positions of Ag NPs, it is shown that the photocurrent density of Mo, W: BVO/Ag NPs-S is lower than that of Mo, W: BVO/Ag NPs-I. The appearance of the oxidation peak of the LSV curve in Mo, W: BVO/Ag NPs-S also proves that the composite structure provides a good chemical environment for embedded Ag NPs.
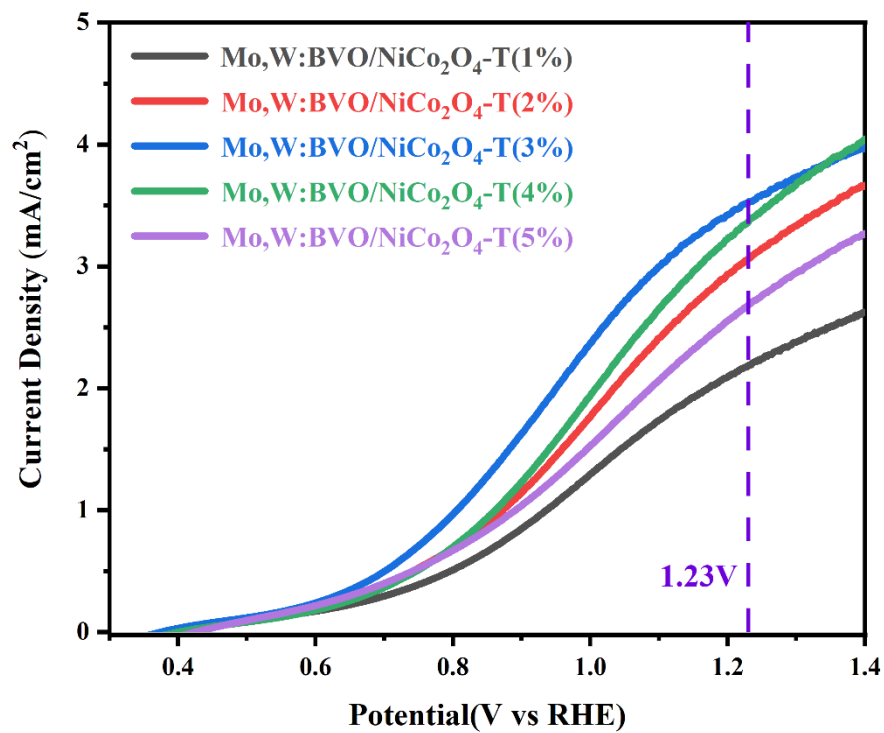
Fig.S11. LSV curves of Mo, W: $BVO/NiCo_2O_4$-T by different content of the $NiCo_2O_4$.
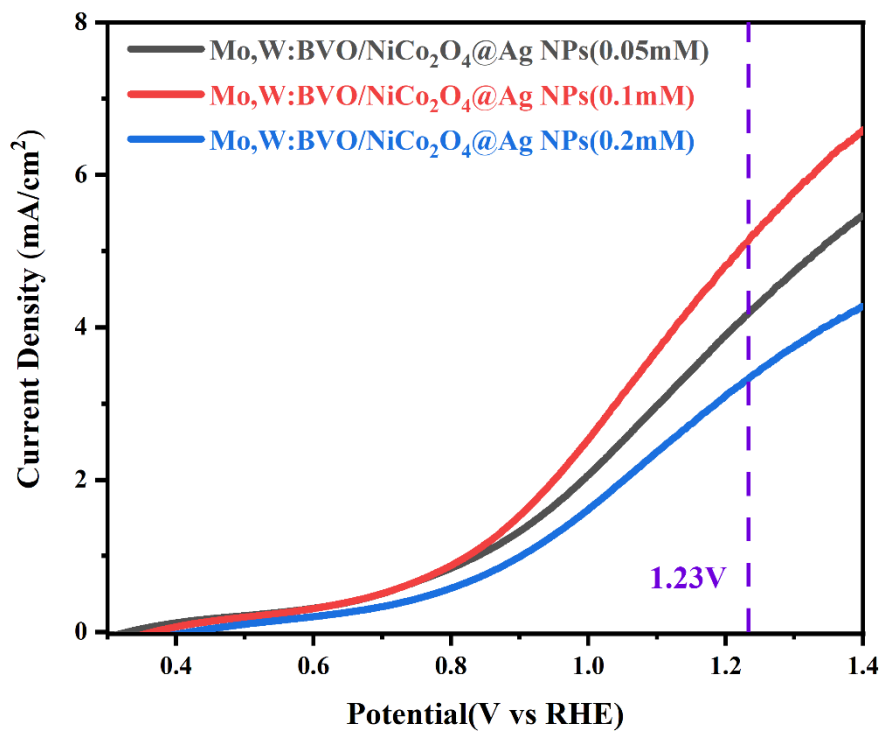
Fig.S12. LSV curves of Mo, W: $BVO/NiCo_2O_4/Ag$ NPs by different concentrations of the $AgNO_3$ solution.
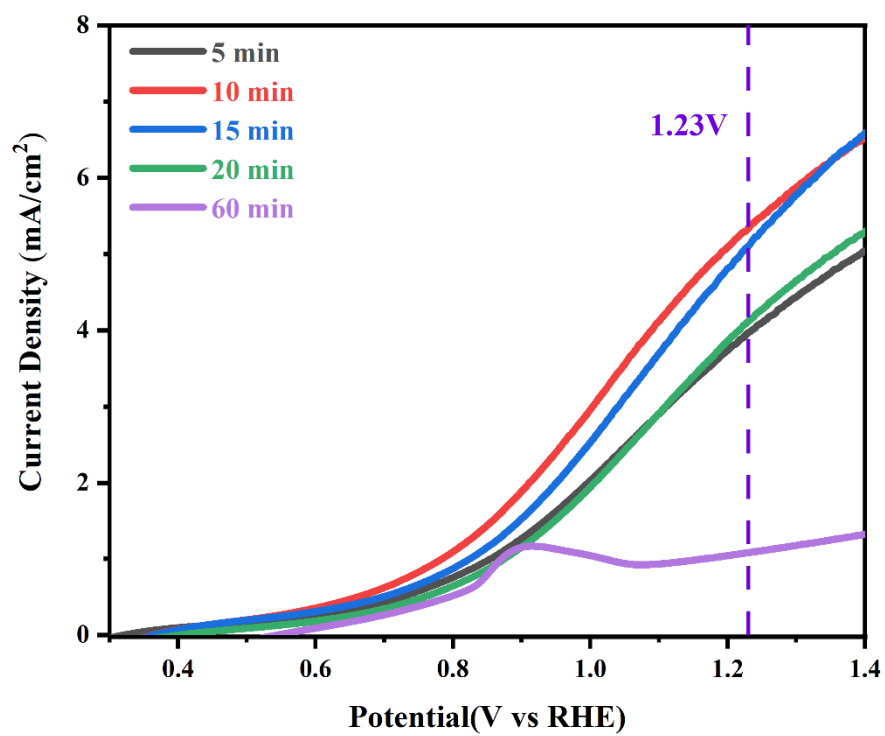
Fig.S13. LSV curves of Mo, W: BVO/NiCo$_2$O$_4$/Ag NPs with different light deposition time in 0.1mM AgNO$_3$ solution.
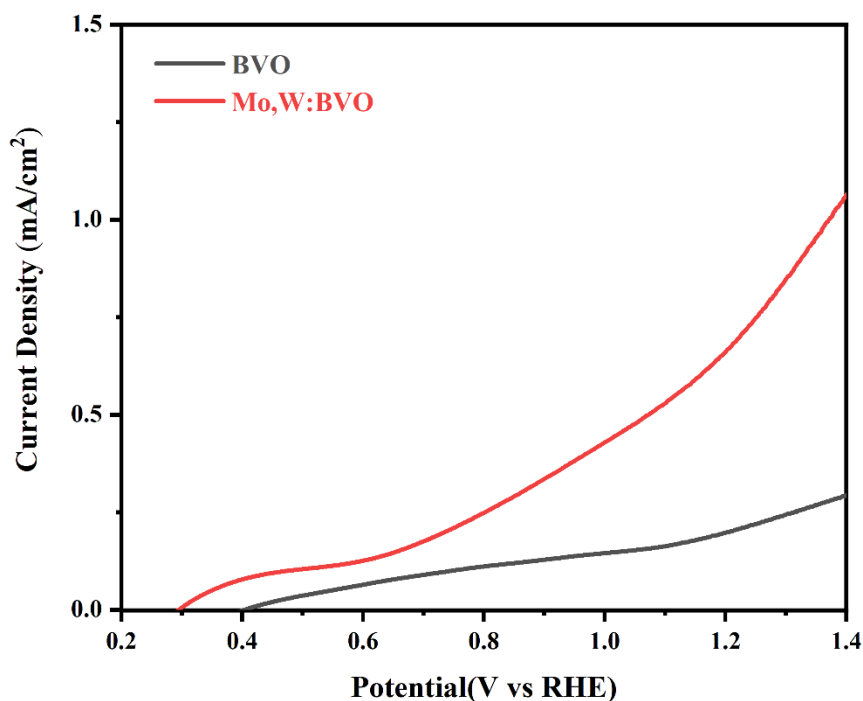
Fig. S14. LSV curve of BVO and Mo and W doped BVO.

As shown in Fig. S15, the photocurrent density of Mo and W co-doped BVO is larger than that of pure BVO, which suggests that the simultaneous doping of Mo and W improves the photo-electrocatalytic performance of pure BVO, and they have a synergistic effect. The high rate of photogenerated carrier complexation in pure BVO leads to its poor photoelectrochemical performance, and the co-doping of Mo and W can improve the electrical conductivity of the material; improve the charge carrier separation of BVO, and the dopant elements can act as traps for electrons or holes, which can help to reduce the complexation of charge carriers, enhance the efficiency of the separation of electrons and holes, and increase the efficiency of the photocatalytic process, which will in turn improve the photoelectrochemical performance, such as the enhancement of the photocurrent intensity and improved photoelectric conversion efficiency.
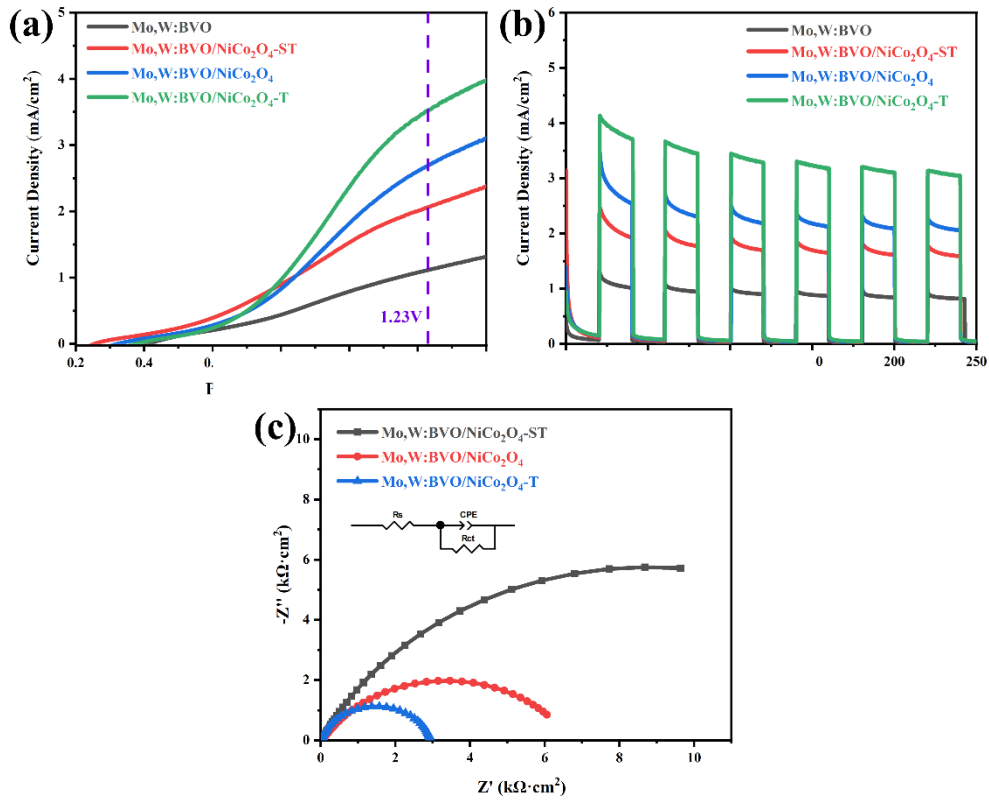
Fig.S15. (a) LSV curves of Mo, W: BVO/NiCo$_2$O$_4$ with different morphologies, (b) i-t stability tests measured, (c) Nyquist plots of the EIS spectra. Inset shows the equivalent model. All the measurements were carried in 0.1 M Na$_2$SO$_4$ (pH=7) electrolyte.
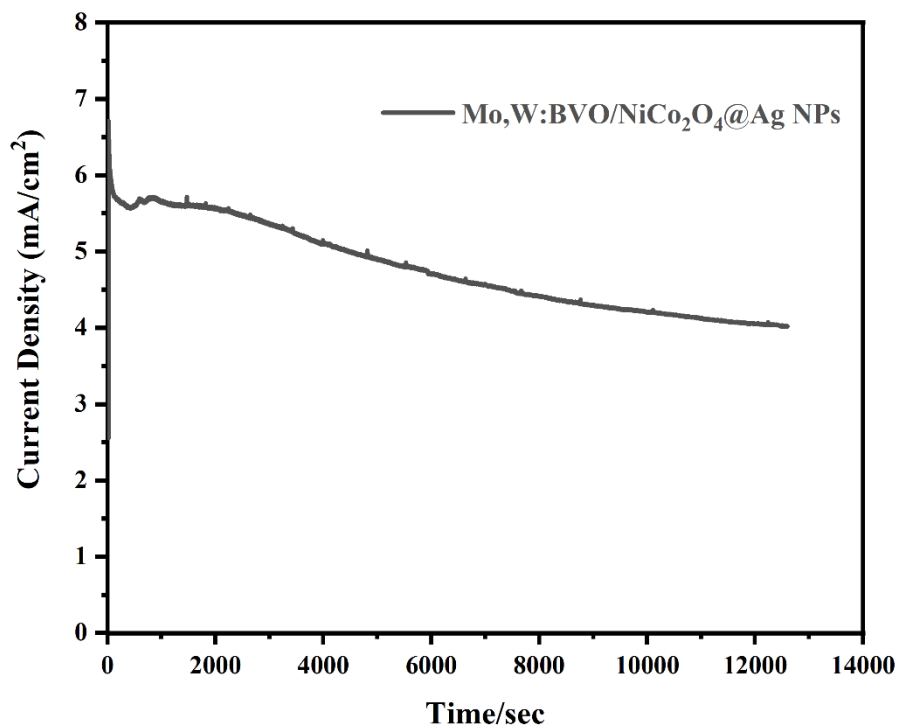
Fig.S16. Stability curves of Mo, W: BVO/NiCo$_2$O$_4$/Ag NPs under AM 1.5 G.

during the long-term stability tests, the photoanodes experienced photocorrosion effects that led to partial dissolution of vanadium ions, which resulted in reduced photostability.

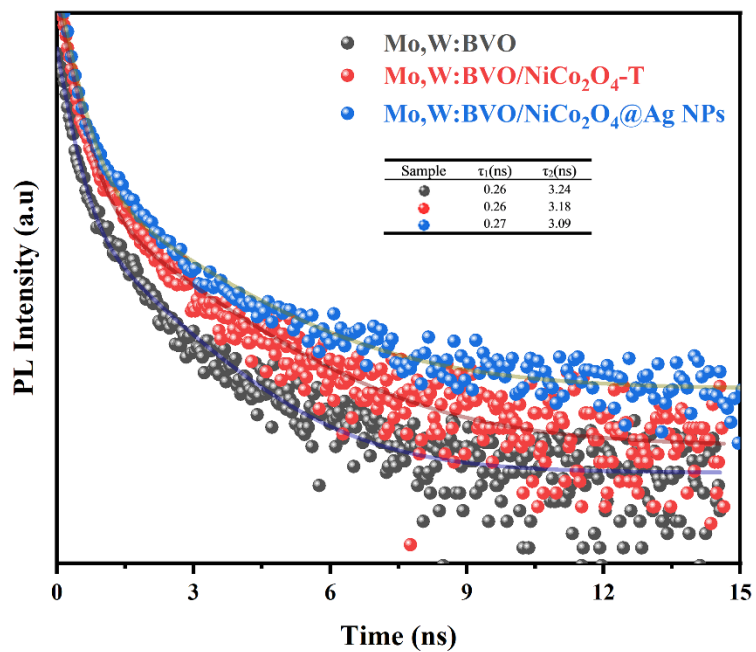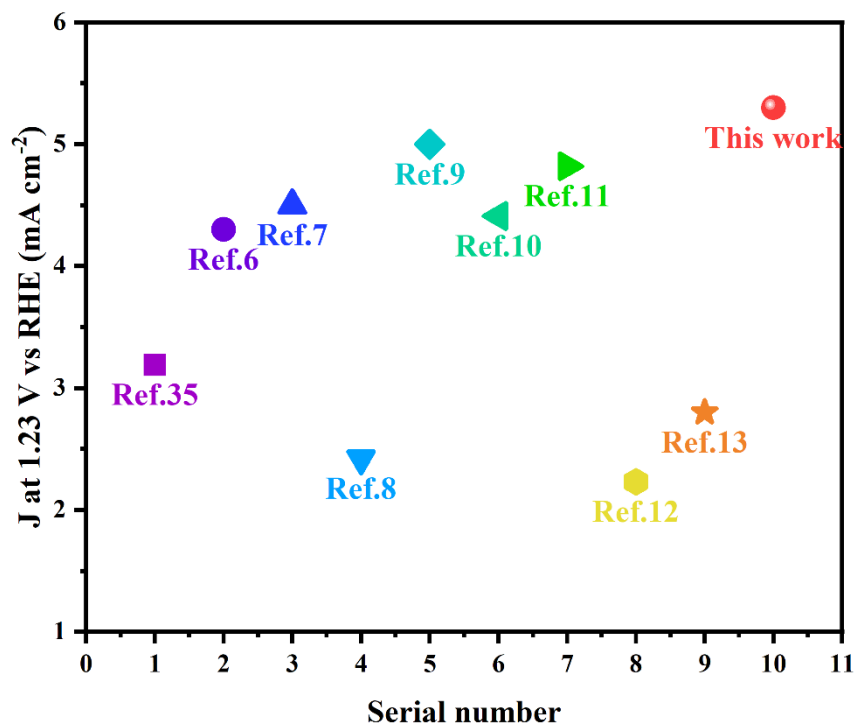**Fig.S17.** time-resolved photoluminescence (TRPL) emission spectra of Mo, W: BVO-based samples.

Fig.S18. Comparison of photocurrent densities of different BVO-based composite photoanodes based on previous reports.

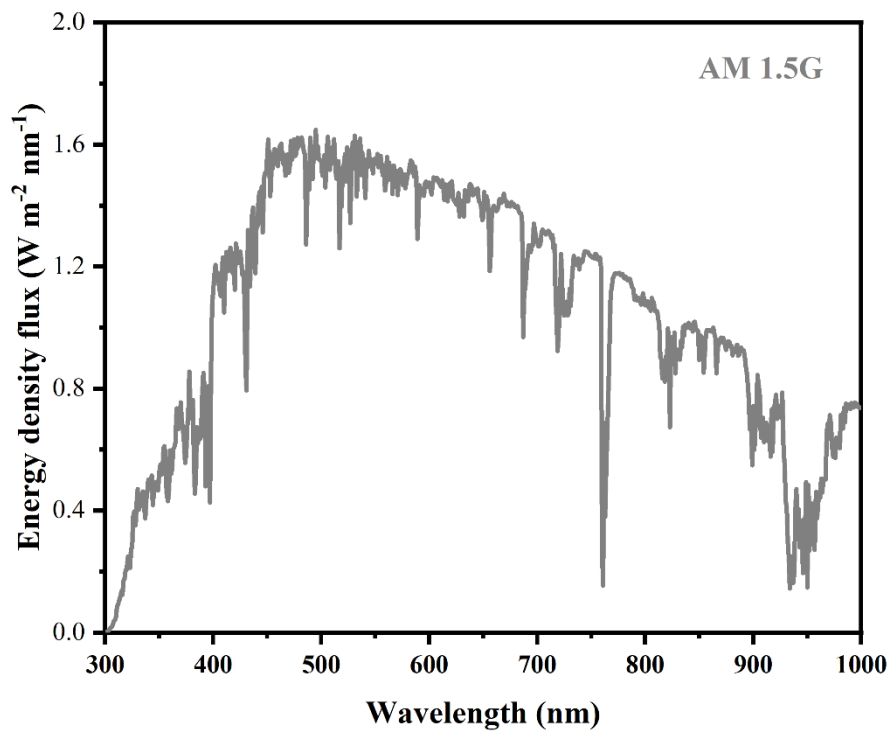**Fig.S19.** AM 1.5G Solar spectrum.

Table.S1. EIS fitting results of Mo, W: BVO-based composite photoanodes.

sample	R_S (Ω)	CPE-T	CPE-P	R_{CT} (Ω)
Mo, W: BVO	32.17	4.660E-05	0.93662	18618
Mo, W: BVO/NiCo$_2$O$_4$-T	17.3	1.480E-04	0.83539	2939
Mo, W: BVO/NiCo$_2$O$_4$@Ag NPs	13.52	2.916E-04	0.7891	1287

Table.S2. Comparison of Our Results with Recent Typical BiVO$_4$-Based Photoanodes

Samples	J (mA·cm^{-2})	electrolyte	light sources	References
BiVO$_4$/Ag/FeOOH	3.19	0.1 M PB (pH=7)	300 W Xe lamp AM 1.5G	7
Ag-HSN/BiVO4	4.30	0.5 M Na$_2$SO$_4$ (pH=7)	300 W Xe lamp AM 1.5G	8
NiCo$_2$O$_4$/Mo: BiVO$_4$	4.5	0.5 M KH$_2$PO$_4$ (pH=7)	300 W Xe lamp AM 1.5G	9
BiVO$_4$-C/N-Ag	2.42	0.5 M Na$_2$SO$_4$ (pH=7)	300 W Xe lamp AM 1.5G	10
BiVO$_4$/Co-Sil (CA)	5.0	0.5 M KBi (pH = 9.5)	300 W Xe lamp AM 1.5G	11
Ni/BiVO$_4$@NiOOH	4.41	0.1 M Na$_2$SO$_4$ (pH=7)	300 W Xe lamp AM 1.5G	12
HT-BiVO$_4$-NiFeOx	4.82	0.1 M KBi (pH=9.5)	300 W Xe lamp AM 1.5G	13
BiVO$_4$-Ni/Co$_3$O$_4$	2.23		300 W Xe lamp AM 1.5G	14
MCo$_2$O$_4$ (M = Mn, Zn)/BiVO$_4$	2.8	0.5 M KH$_2$PO$_4$ (pH=7)	300 W Xe lamp AM 1.5G	15
Mo, W: BVO/NiCo$_2$O$_4$@Ag NPs	5.3	0.1 M Na$_2$SO$_4$ (pH=7)	300 W Xe lamp AM 1.5G	This work.

1. L. Yang, R. Wang, N. Zhou, D. Liang, D. Chu, C. Deng, H. Yu and J. Lv, *Journal of Colloid and Interface Science*, 2023, **631**, 35-45.
2. S. Liu, R.-T. Gao, R. Zhang, Z. Wang, X. Liu, T. Nakajima, X. Zhang, Y. Su and L. Wang, *Applied Catalysis B: Environmental*, 2021, **298**, 120610.
3. J. Zhang, X. Wei, J. Zhao, Y. Zhang, L. Wang, J. Huang, H. She and Q. Wang, *Chemical Engineering Journal*, 2023, **454**, 140081.
4. B. Jin, Y. Cho, Y. Zhang, D. H. Chun, P. Li, K. Zhang, K.-S. Lee and J. H. Park, *Nano Energy*, 2019, **66**, 104110.
5. H. Zhang and C. Cheng, *ACS Energy Letters*, 2017, **2**, 813-821.
6. K. Chang, M. Li, T. Wang, S. Ouyang, P. Li, L. Liu and J. Ye, *Advanced Energy Materials*, 2015, **5**.
7. X. Gu, J. Zhang, L. Hou, X. Fu, X. Yu, Y. Zhu and Y. Zhang, *Surfaces and Interfaces*, 2021, **25**.
8. A. Tavazohi, H. Abdizadeh and M. R. Golobostanfard, *International Journal of Hydrogen Energy*, 2022, **47**, 18992-19004.
9. C. Feng, Q. Zhou, B. Zheng, X. Cheng, Y. Zhang and Y. Bi, *Journal of Materials Chemistry A*, 2019, **7**, 22274-22278.
10. P. Guan, H. Bai, F. Wang, H. Yu, D. Xu, W. Fan and W. Shi, *Chemical Engineering Journal*, 2019, **358**, 658-665.
11. Q. Sun, T. Cheng, Z. Liu and L. Qi, *Applied Catalysis B: Environmental*, 2020, **277**.
12. P. Wen, R. Lei, X. Cao, Q. Ma, G. Zhang, C. Guo, X. Wang and Y. Qiu, *Chemical Engineering Journal*, 2023, **454**.
13. Q. Wang, L. Wu, Z. Zhang, J. Cheng, R. Chen, Y. Liu and J. Luo, *ACS Appl Mater Interfaces*, 2022, DOI: 10.1021/acsami.2c02790.
14. H. Bai, X. Li, Y. Zhao, W. Fan, Y. Liu, Y. Gao, D. Xu, J. Ding and W. Shi, *Applied Surface Science*, 2021, **538**.
15. D. Xu, T. Xia, H. Xu, W. Fan and W. Shi, *Chemical Engineering Journal*, 2020, **392**.